applied optics

Comparison of image reconstruction techniques for optical projection tomography

Anna K. Trull,[1,*] Jelle van der Horst,[1] Lucas J. van Vliet,[1] and Jeroen Kalkman[1,2]

[1]Department of Imaging Physics, Delft University of Technology, Lorentzweg 1, 2628 CJ Delft, The Netherlands
[2]e-mail: j.kalkman@tudelft.nl
*Corresponding author: a.k.trull@tudelft.nl

Received 14 November 2017; revised 11 January 2018; accepted 29 January 2018; posted 30 January 2018 (Doc. ID 309822); published 7 March 2018

We present a comparison of image reconstruction techniques for optical projection tomography. We compare conventional filtered back projection, sinogram filtering using the frequency–distance relationship (FDR), image deconvolution, and 2D point-spread-function-based iterative reconstruction. The latter three methods aim to remove the spatial blurring in the reconstructed image originating from the limited depth of field caused by the point spread function of the imaging system. The methods are compared based on simulated data, experimental optical projection tomography data of single fluorescent beads, and high-resolution optical projection tomography imaging of an entire zebrafish larva. We demonstrate that the FDR method performs poorly on data acquired with high numerical aperture optical imaging systems. We show that the deconvolution technique performs best on highly sparse data with low signal-to-noise ratio. The point-spread-function-based reconstruction method is superior for nonsparse objects and data of high signal-to-noise ratio.

OCIS codes: (100.3010) Image reconstruction techniques; (100.3190) Inverse problems; (100.6950) Tomographic image processing.

https://doi.org/10.1364/AO.57.001874

1. INTRODUCTION

For the study of biological samples and small animals, such as zebrafish or (mouse) embryos, optical tomographic imaging techniques, such as optical diffraction tomography [1] and optical projection tomography (OPT) [2], are among the standard imaging modalities. From these samples, projections of transmitted or emitted (fluorescence) light are recorded. From these projections, an image of the object is reconstructed using tomographic reconstruction techniques. In OPT, a lens-based optical imaging system is used to image the sample onto the detector. The optical system is characterized by the point spread function (PSF). Due to light diffraction, instead of collecting light along a straight path (line) through the object, light from a sample volume, determined by the shape of the PSF, is collected by the detector. For image acquisition with high numerical aperture (NA), small depth of focus lenses, this results in efficient light collection from the focal plane. However, light from regions far from the focal plane is inefficiently collected. Standard reconstruction techniques, such as filtered back projection (FBP), are based on straight ray approximation, which neglects the effect of light diffraction by the imaging lens [3]. Consequently, OPT images reconstructed with FBP can suffer from severe image degradation.

Reconstruction algorithms that include the PSF in the reconstruction have been developed for clinical tomographic imaging techniques such as PET [4], SPECT [5], and x-ray CT [6]. Also, for optical tomographic imaging, various reconstruction techniques were developed to correct for the effect of the PSF, as indicated in Fig. 1, where these techniques are divided in three categories. First, correction for the effect of the PSF can take place before the reconstruction, either by filtering the sinogram in real space using an iterative deconvolution [7] or by filtering the sinogram in Fourier space with a filter based on the frequency–distance relation [8,9]. In both cases, these methods are directly applied to the measured projection data, and the processed sinogram is converted to an image using FBP. Second, correction for the effect of the PSF can take place after reconstruction using deconvolution of the image reconstructed with FBP [10]. Third, we recently demonstrated correction for the effect of the PSF during the tomographic reconstruction process itself using iterative optimization [11].

In this work, we compare three advanced tomographic reconstruction methods, namely frequency–distance relationship (FDR) followed by FBP [9], FBP followed by image deconvolution [10], and 2D PSF-based reconstruction [11] that all correct for the effect of the optical PSF, with the classical FBP [3]. First, we test all methods on their ability to reduce tangential blurring in the reconstructed image using simulated

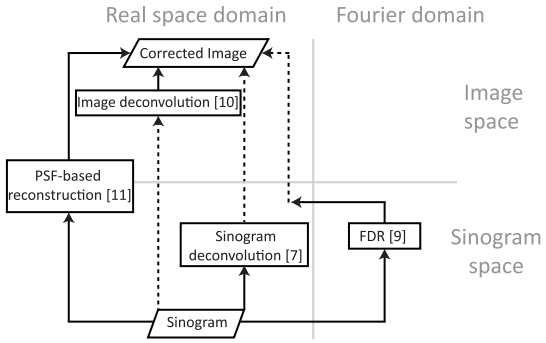

Fig. 1. Schematic overview of different tomographic reconstruction methods that correct for the PSF [7,9910–11]. The left-hand side indicates that the reconstruction is performed in real space, and the right-hand side indicates that it is performed in Fourier space. The bottom side indicates that the reconstruction is performed in sinogram space, and the top side indicates that it is performed in image space. The dashed lines indicate conventional FBP reconstruction.

data. In these simulation experiments, we study the effect of the signal-to-noise ration (SNR) and numerical aperture on the reconstruction error. Second, we compare the performance of all reconstruction algorithms on experimental data. Since no reference image is available for experimental data, a no-reference or blind image quality assessment (NR-IQA) is performed to provide an image quality measure that enables quantitative comparison of the quality of the different reconstruction techniques. Finally, we indicate which algorithm to choose for objects that have different signal-to-noise ratio and/or are imaged with different numerical apertures.

2. THEORY OF TOMOGRAPHIC IMAGE RECONSTRUCTION

A. General Problem Formulation

For the imaging geometry of OPT, see Fig. 2(a), light from the object is imaged from the sample onto the detector using lenses. As a result, the image of a point source gives a blurred spot on the detector determined by the PSF $h(x, y, z)$. In general, the shape of the 3D PSF can be complicated as it is dependent on the exact imaging geometry. It can be obtained using Fourier optics calculations, optical simulations, or experimental measurement. For the case of incoherent imaging of an object of which its structure varies slowly in the y direction, it was shown [10,11] that the projections are given by the convolution of the 2D object $f(x, z)$ by the 2D PSF $|h(x, z)|^2$ as

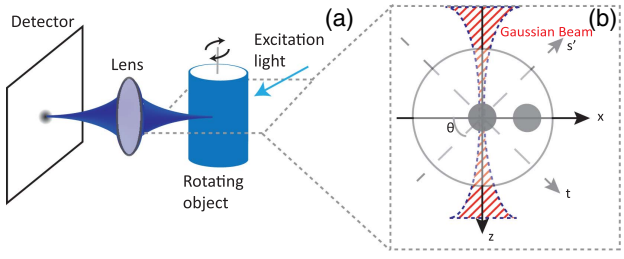

Fig. 2. (a) Schematic overview of the optical projection tomography fluorescence imaging geometry. (b) 2D slice of the object and the Gaussian beam. The rotation angle is denoted by θ.

$$p(s,\theta) = \int_{-\infty}^{\infty}\int |h(x\cos\theta + z\sin\theta - s, x\sin\theta + z\cos\theta)|^2 \times f(x,z)\mathrm{d}x\mathrm{d}z, \quad (1)$$

where $|h(x, z)|^2$ is the spatially variant incoherent PSF, s the lateral shift, and $\theta \in [0, 2\pi]$ the rotation angle. Equation (1) shows that the measured intensity on the detector is given by an integral over the object, which is illustrated in Fig. 2(b). To facilitate a quantitative comparison of the different reconstruction algorithms, we use a 2D Gaussian PSF that is described by

$$|h(x,z)|^2 = \left| \frac{1}{\sqrt{1+\left(\frac{z}{z_R}\right)^2}} \exp\left(-\frac{x^2}{w_0^2\left(1+\left(\frac{z}{z_R}\right)^2\right)}\right)\right|^2, \quad (2)$$

where $z_R = \pi w_0^2/\lambda$ is the Rayleigh range, w_0 the Gaussian beam waist, and λ the wavelength. For a Gaussian PSF, both the FDR filter and the image deconvolution filter [10] can be analytically calculated. This enables a quantitative comparison. However, the general results of our comparison hold for arbitrary beam shapes if correctly implemented in the corresponding reconstruction algorithm.

B. FBP Reconstruction

Due to its fast reconstruction time and the easy concept, FBP reconstruction is still the most commonly used reconstruction technique in optical tomography. In FBP, a straight ray geometry is used over which the measured projection is back projected onto the object. FBP is the correct reconstruction for the case of an ideal imaging system where the PSF is described by $|h(x, z)|^2 = \delta(x)$. This means that irrespective of the distance of the object to the collection system, the signal from all pixels on a line through the object is collected onto a single detector pixel. For $|h(x, z)|^2 = \delta(x)$, Eq. (1) results in the standard Radon transform [3,12],

$$p(s,\theta) = \int_{-\infty}^{\infty}\int f(x,z)\delta(x\cos\theta + z\sin\theta - s)\mathrm{d}x\mathrm{d}z. \quad (3)$$

In this case, the object can be retrieved by FBP as

$$f(x,z) = \int_0^{\pi}\int_{-\infty}^{\infty} P_\theta(f_s)\exp(i2\pi f_s s)|f_s|\mathrm{d}f_s\mathrm{d}\theta, \quad (4)$$

where $P_\theta(2\pi f_s)$ is the 1D Fourier transform of the projection data at angle θ. However, in case the PSF is not ideal, FBP reconstruction causes artifacts and/or severe blurring in the reconstructed image. Next, we describe three algorithms that incorporate the PSF before (FDR), after (image deconvolution) or during the image reconstruction (PSF-based reconstruction).

C. FDR Reconstruction

Originating from the field of x-ray CT, reconstruction methods that take the PSF into account are algorithms based on the FDR [8,9,13]. FDR has been implemented for reconstructions of OPT tomograms corrected for the out-of-focus deterioration of resolution due to the imaging system [8]. In FDR, the blurring of the sinogram in the Fourier domain is described by

$$P_b(f_x, f_y) = H(f_x, f_y)P_o(f_x, f_y), \quad (5)$$

where $P_b(f_x, f_y)$ is the Fourier transform of the blurred sinogram, $H(f_x, f_y)$ is the filter based on the PSF describing the blurring, and $P_o(f_x, f_y)$ is the Fourier transform of the sinogram of the object with spatial frequencies f_x and f_y. The system PSF is used to create an inverse filter $H^{-1}(f_x, f_y)$ that is multiplied with the Fourier transform of the sinogram to remove the blurring caused by $H(f_x, f_y)$ [13,14]. For the Gaussian PSF in Eq. (5), the filter $H(f_x, f_y)$ is given by

$$H(f_x, f_y) = \frac{1}{\left(1 + \frac{\lambda^2 f_y^2}{f_x^2 \pi^2 w_0^2}\right)\sqrt{\frac{w_0}{\frac{\lambda^2 f_y^2}{f_x^2} + \pi^2 w_0^2}}} \times \exp\left(-\frac{f_x}{8}\left(\frac{\lambda^2 f_y^2}{f_x^2 \pi^2 w_0} + f_x \pi w_0^2\right)\right). \quad (6)$$

1. Analytical Derivation of the FDR Filter for a Gaussian PSF

In the following, we derive the analytical inverse filter $H(f_x, f_y)^{-1}$. Let us assume a point source object located on the x axis at distance l from the origin defined as

$$f(x, z) = \delta(x - l)\delta(z). \quad (7)$$

The PSF is defined as in Eq. (2). The blurred sinogram is then defined as

$$p_b(s, \theta) = \iint \delta(x - l\cos\theta)\delta(z) \times |h(x\cos\theta + z\sin\theta - s, x\sin\theta + z\cos\theta)|^2 \mathrm{d}x\mathrm{d}z.$$

Integration over x and z, with $|h(x, z)|^2$ described by Eq. (2), leads to

$$p_b(s, \theta) = \frac{1}{1 + \frac{l^2\lambda^2\sin^2\theta}{\pi^2 w_0^2}} \exp\left(-\frac{2(s - l\cos\theta)^2}{w_0\left(1 + \frac{l^2\lambda^2\sin^2\theta}{\pi^2 w_0^2}\right)}\right). \quad (8)$$

The Fourier transform of the $p_b(s, \theta)$ [14] is given by

$$P_b(f_x, f_y) = \frac{1}{2\pi}\int_0^{2\pi}\int_{-\infty}^{\infty} p_b(s, \theta)\exp(-j(f_x s + f_y\theta))\mathrm{d}s\mathrm{d}\theta. \quad (9)$$

Inserting Eq. (8) in Eq. (9) and integration over s leads to

$$P_b(f_x, f_y) = \frac{1}{2\pi}\int_0^{2\pi} \frac{1}{2\pi\left(1 + \frac{\lambda^2 f_y^2}{f_x^2\pi^2 w_0^2}\right)\sqrt{\frac{w_0}{\frac{\lambda^2 f_y^2}{f_x^2} + \pi^2 w_0^2}}} \times \exp\left(-\frac{f_x}{8}\left(f_x\pi^2 w_0^2 - 8jl\cos\theta + \frac{f_x l^2\lambda^2\sin^2\theta}{\pi^2 w_0^2}\right)\right) \times \exp(-jf_y\theta))\mathrm{d}\theta. \quad (10)$$

An expression for the filter can be derived by assuming a stationary phase approximation, i.e., the function $\exp(-jf_y\theta + jf_x l\cos\theta)$ only takes on a nonzero value if the derivative of this angle with respect to θ is zero, i.e.,

$$\frac{d}{d\theta} f_y\theta - f_x l\cos\theta = f_y + f_x l\sin\theta = 0, \quad (11)$$

which is equivalent to $l\sin\theta = -\frac{f_y}{f_x}$. Evaluating this in Eq. (10) gives

$$P_b(f_x, f_y) \approx \frac{1}{2\pi\left(1 + \frac{\lambda^2 f_y^2}{f_x^2\pi^2 w_0^2}\right)\sqrt{\frac{w_0}{\frac{\lambda^2 f_y^2}{f_x^2} + \pi^2 w_0^2}}} \times \exp\left(-\frac{f_x}{8}\left(\frac{\lambda^2 f_y^2}{f_x^2\pi^2 w_0} + f_x\pi^2 w_0^2\right)\right) \times \left[\int_{\theta_1-\varepsilon}^{\theta_1+\varepsilon}\exp(g)\mathrm{d}\theta + \int_{\theta_2-\varepsilon}^{\theta_2+\varepsilon}\exp(g)\mathrm{d}\theta\right], \quad (12)$$

where $g = -j(f_x l\cos\theta + f_y\theta)$. From a similar derivation for an ideal imaging system, which only contains the last term of Eq. (12) and using Eq. (5), it can be derived that the unblurring FDR filter is

$$H^{-1}(f_x, f_y) = \left(1 + \frac{\lambda^2 f_y^2}{f_x^2\pi^2 w_0^2}\right)\sqrt{\frac{w_0}{\frac{\lambda^2 f_y^2}{f_x^2} + \pi^2 w_0^2}} \times \frac{1}{\exp\left(\frac{f_x}{8}\left(\frac{\lambda^2 f_y^2}{f_x^2\pi^2 w_0} + f_x\pi^2 w_0^2\right)\right)}. \quad (13)$$

D. Image Deconvolution

A general approach for PSF correction is image deconvolution. However, in case of tomographic reconstruction, the PSF of the reconstructed image is a complicated expression of the PSF of the imaging system with which the projections are measured. For a Gaussian beam, the 2D PSF of the FBP reconstructed image is spatially varying with the coordinate x and coordinate y according to

$$\mathrm{PSF}(x, y) = \mathcal{R}_{-\theta}\left(\sqrt{\frac{1}{\pi^2 a_y a_x}}\exp\left(-\left[\frac{x^2}{a_x} + \frac{y^2}{a_y}\right]\right)\right). \quad (14)$$

In Eq. (14) $a_x = w_0^2/2$ and $a_y = (w_0^2 + \frac{\lambda^2 r_0^2}{\pi^2 w_0^2})/2$, r_0 is the location of the PSF in the image domain and $\mathcal{R}_{-\theta}$ is an operator to perform a standard coordinate transformation over an angle [10]. From Eq. (14) it can be observed that the resolution in the tangential direction deteriorates with increasing distance to the rotation axis, whereas the resolution in the radial direction is constant. Using a conversion to polar coordinates, the image can be successively deconvolved in the radial and angular direction using deconvolution (e.g., with the Lucy–Richardson algorithm).

E. PSF-Based Reconstruction

An advanced reconstruction method is based on the inclusion of the imaging system's PSF into the tomographic reconstruction [11]. Given the measured projections $\mathbf{p}$ and the effect of imaging system PSF given by Eq. (2) as described by matrix $\mathbf{A}$, the object $\mathbf{f}$ can be reconstructed by solving

$$\underset{\mathbf{f}}{\mathrm{argmin}}\frac{1}{2}\|\mathbf{A}\cdot\mathbf{f} - \mathbf{p}\|_2^2, \quad (15)$$

where $\|\cdot\|_2^2$ denotes the Euclidean norm. Equation (15) can be solved using the least-squares optimization method.

3. METHODS

A. Reconstruction Algorithms

All tomographic reconstructions are performed on a computer with an Intel(R) Xeon(R) CPU Processor (E5-1620 v3 at

3.50 GHz), 32 GB installed memory, and a 64-bit operating system. The data are processed using software written in the commercial software package MATLAB (Mathworks, R2016a)(Our code to perform these calculations is available on request.). The reconstructions with FBP are done with the MATLAB function *iradon*. The FDR method is implemented using the analytical expression for the inverse filter $H^{-1}(f_x, f_y)$, derived in Section 2.C.1. After the FDR reconstruction, intensity thresholding is applied to remove reconstruction artifacts. The thresholding is done individually for each dataset. For the simulations, a thresholding of 0.04 (15.7% of the peak value) is used. For the zebrafish dataset, the threshold is set to 0.1 (2.5% of the peak value).

The deconvolution and the PSF-based method implementations are identical to the original implementation of the methods [10,11]. To enable a quantitative comparison of the reconstructed images, all reconstructed images are scaled using the scaling described in [11].

B. Image Quality Assessment

For both simulated and experimental data of point objects, the image quality is determined from the width of the PSF in the reconstructed image. The full width at half maximum (FWHM) is obtained from a bivariate Gaussian fit in a region of interest around the image of isolated single objects with the width in the two perpendicular dimensions as independent fit parameters.

Since no reference image is available for experimental data of spatially extended objects, an NR-IQA is used to compare the quality of the different reconstruction results. NR-IQA aims to determine quantitative measures to objectively predict the quality of an image based only on the image itself [15]. In our comparison, we use the SNR and the sharpness provided by NR-IQA to assess the quality of the reconstructed images.

It is assumed that both the image quality increases with increasing SNR and image sharpness. In case of suboptimal performance, both these metrics are lower. The SNR of an image is defined as

$$\mathrm{SNR} = 20\,\log\left(\frac{\mu_{\mathrm{signal}}}{\sigma_{\mathrm{noise}}}\right), \tag{16}$$

where μ_{signal} is the average image intensity in a signal mask region and σ_{noise} is the standard deviation of the image intensity in a noise region. The latter corresponds to the region outside the signal mask [16].

First, a signal and a background mask are created for the image reconstructed with every method. The signal mask comprises all pixels whose intensity is higher than the average background signal plus four times its standard deviation. The background mask is defined as the area of the image that is not in the signal mask. Hence, in the background mask the image intensity is smaller than the average background signal plus four times its standard deviation. Second, the intersection of the signal masks and background masks for all four reconstruction methods are estimated. This final signal mask is then used to estimate the intersection signal in the image. The final background mask is used to estimate the standard deviation of the background, which we use as a measure of the noise. We use the intersection masks, since no ground truth of the signal and noise regions is available. Hence, the intersection masks weigh each method in the same way in the determination of the SNR.

Following the definition of De and Masilamani [17], the sharpness in the image is defined in the frequency domain of the image as the ratio FM according to

$$\mathrm{FM} = \frac{T}{M \cdot N}, \tag{17}$$

where T denotes the total number of pixels in the Fourier transform of the image that have a magnitude larger than the maximum magnitude divided by 1000. The Fourier-transformed image is centered so that the zero-frequency components are represented in the center of the spectrum. The denominator contains the product of the image size of M times N in the two dimensions. The use of the metric of Eq. (17) for image quality assessment is based on the assumption that a sharper image will have a larger number of high-frequency components in the frequency domain compared to a blurred image, which has mainly low-frequency components.

C. Tomographic Reconstruction Simulations

Multiple images of size 5×5 mm^2 (300 by 300 pixels) are generated with a circular Gaussian-shaped object placed at a specific distance from the origin in every image. The objects have an FWHM in the x and y direction of 125 μm. The object in the first image is located in the center of the image, and the object in the last image is located horizontally close to the edge of the image. The Gaussian PSF is implemented for NA = 0.027 and NA = 0.053 and with a beam waist of $w_0 = 6$ μm. The depth of field (DOF), defined as twice the Rayleigh length, for NA = 0.027 is DOF = 48 μm and for NA = 0.053, DOF = 24 μm. The sinogram is blurred with the Gaussian PSF and then used as input for the different reconstruction algorithms. After reconstruction, a Gaussian is fitted to each reconstructed object, and the FWHM of the object in the radial and tangential direction is determined. Deconvolution of the FBP-reconstructed image is performed with the MATLAB function *deconvlucy*, with the number of iterations set to 100. The maximum number of iterations of the PSF-based algorithm for an NA of 0.027 is set to 4000, and for an NA of 0.053 to 6000. The convergence and optimal number of iterations is object, NA, and SNR dependent. For both the deconvolution and PSF-based reconstruction, convergence of the method for the indicated number of iterations is validated visually. The absolute error of the projections is estimated as $||\mathbf{Af} - \mathbf{p}||_2^2$, where $\mathbf{A}$ denotes the geometry matrix, $\mathbf{f}$ the reconstructed image, and $\mathbf{p}$ the projections with added noise.

4. RESULTS

A. Image Reconstruction Comparison of Simulations

Figure 3 shows the reconstruction as well as the tangential and radial FWHM of the object located at a varying radial distance to the center of the image. A sharp image on the detector is made for radial distance 0, which is the center of rotation. In Fig. 3(a) the original image and the reconstruction results using FBP, FDR, image deconvolution, and PSF-based reconstruction are shown for an NA of 0.027. It is clear that

the FBP-reconstructed image is severely blurred, especially for objects far from the center. The FDR method produces side lobes in the radial and tangential direction and has a lower peak intensity. Both deconvolution and PSF-based reconstruction show a clear reduction in tangential blurring compared to FBP. Figure 3(b) shows the fitted FWHM of the objects for an NA = 0.027. The optimal resolution of the reconstruction is determined by the sum of the variance of the PSF and of the object, subsequently converted to FWHM, which is indicated for the tangential and radial directions. For the FBP reconstruction, the width in the tangential direction increases significantly and follows the theoretical prediction. The FDR method shows a significantly improved result, albeit slightly above the fundamental limit for larger distances to the origin. For small distances to the origin, it is lower than the theoretical minimum. This difference is within the resolution of the simulation and attributed to the non-Gaussian shape of the FDR-reconstructed objects (e.g., the presence of side lobes). The image deconvolution method and the PSF-based reconstruction technique show an almost full reduction of the tangential blurring for all radial distances. In the radial direction, all algorithms achieve diffraction-limited resolution. A comparison of the PSF in the tangential direction is shown in Fig. 3(c) for an object at a distance of 2 mm from the center. In Fig. 3(d), the original image and the reconstruction results using FBP, FDR, image deconvolution, and PSF-based reconstruction are shown for NA = 0.053. For this higher NA, the FBP-reconstructed image shows a stronger burring than in Fig. 3(a). While deconvolution and PSF-based reconstruction give good results, the FDR method produces side lobes in the radial and tangential direction. Figure 3(e) shows the FWHM of the same objects. The FBP reconstruction shows an increase of the tangential width, which is now even larger for the high NA case. It can be observed that the deconvolution algorithm is able to reduce the tangential blurring, whereas PSF-based reconstruction performs less than ideal at large distances from the center. The FDR gives a significantly larger FWHM, especially at large radial distances from the center. A comparison of the PSF in the tangential direction is shown for a distance of 2 mm from the center in Fig. 3(f).

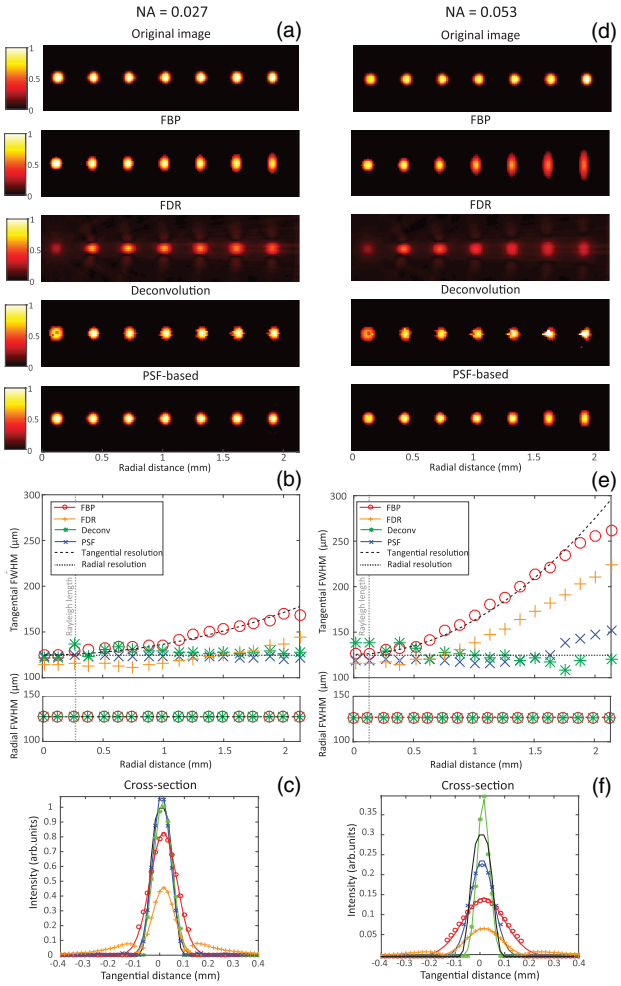

Fig. 3. Comparison of the ground truth and the reconstructed image. (a) The original image, and the reconstructions using FBP, FDR, image deconvolution, and PSF-based reconstruction for a PSF with an NA = 0.027. (b) Tangential and radial FWHM of the cavities for a PSF with an NA = 0.027. (c) Cross section of the reconstructions [shown in (a)] in the tangential direction for a distance of 2 mm from the center. The solid black line indicates the input object. (d) The original image, and the reconstructions, using FBP, FDR, image deconvolution, and PSF-based reconstruction for a PSF with an NA = 0.053. (e) Tangential and radial FWHM of the cavities for a PSF with an NA = 0.053. (f) Cross section of the reconstructions [shown in (d)] in the tangential direction for a distance of 2 mm from the center. The solid black line indicates the input object.

The previous simulations are performed for the noise-free case, i.e., the SNR is infinite. However, the presence of noise influences the reconstruction result. For iterative methods such as deconvolution and the PSF-based reconstruction, the convergence rate and obtained optimal solution depend on the SNR in the projections. The influence of noise on the reconstruction is studied for a single circular-cavity object at a radial distance of 2 mm from the center. Various amounts of noise are added to the projections. Figure 4 illustrates the relation between the absolute error of the projections [according to Eq. (15)] and the number of iterations for a low (top) and a high (bottom) NA. For reconstruction methods based on analytical methods, such as the FBP or FDR, the absolute reconstruction error is similar for low and high SNR (lines overlap in Fig. 4). For both NAs, the deconvolution approach, which takes the FBP as input, gives a lower absolute error compared to FDR and FBP. Although deconvolution is iterative, convergence is already reached after the first iteration. The PSF-based reconstruction has the lowest absolute error compared to the other methods for both high and low NA. For a large number of iterations, an amplification of the reconstruction error can be seen. If not terminated, the reconstruction error for the PSF-based reconstruction grows. It may even exceed that of the other methods. We noted that the number of iterations for which convergence is observed depends on the object to be reconstructed. Hence, the optimum number of iterations needs to be determined for each dataset individually, which is an object-dependent regularization.

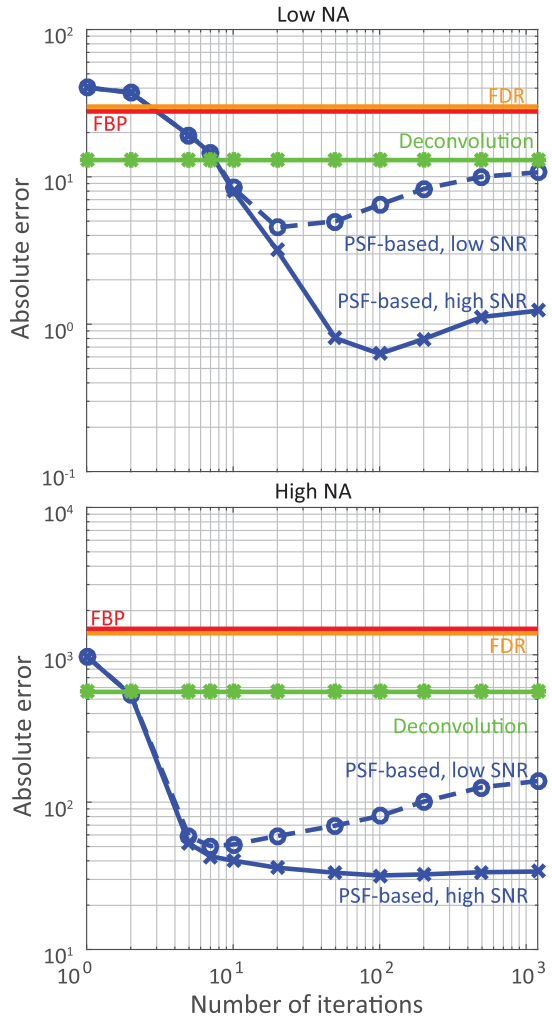

Fig. 4. Reconstruction error for a low NA (top) and a high NA (bottom) optical imaging system for SNR = 40 dB (solid lines) and SNR = 20 dB (dashed lines). PSF-based reconstruction simulations are performed for reconstruction at different SNRs (indicated).

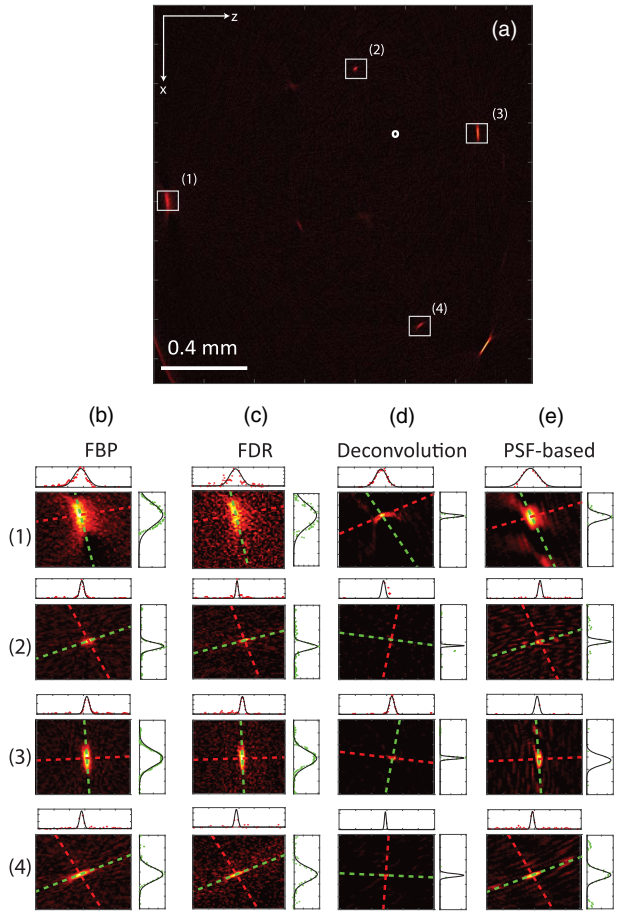

Fig. 5. Reconstructions using FBP, FDR, deconvolution, and PSF-based reconstruction for a single averaged sinogram in the $x - z$ plane. The dash lines indicate the Gaussian fit in radial (red) and tangential direction (green) of fluorescent beads. (a) FBP image reconstruction. (b) Zoom in on individual beads in (a). (c) FDR reconstruction. (d) Image deconvolution. (e) PSF-based reconstruction.

B. Image Quality of Experimental OPT Data

We investigate the reconstruction of single fluorescent bead emitters embedded in an agarose emulsion measured with OPT. The experimental setup is described in more detail in [10], and the main parameters of importance are briefly discussed. The experimentally determined Gaussian PSF has a beam waist in focus of $w_0 = 6$ µm, NA = 0.053, and the measured Gaussian beam shape is used in the PSF-based reconstruction. A sharp image on the detector is made for radial distance 0, which is the center of rotation. The field of view of the experimental data is 5.2 × 5.2 mm^2. In the lateral direction, the detector has 1344 pixels per projection, and 360 projections are acquired over 360 degrees with one-degree spacing. The total dataset consists of 1024 sinograms covering a length of 4 mm along the rotation axis. Subsequently, the 1024 sinograms are combined into 32 averaged sinograms. The preprocessing is described in [11].

Figure 5 shows the reconstructions for a single averaged slice with the different methods. The tangential and radial blurring are clearly visible in Figs. 5(a) and 5(b), where the image is reconstructed with FBP.

For some beads, the FDR reconstruction shows improvement over FBP, as shown in Fig. 5(c). The PSF-based reconstruction, shown in Fig. 5(e), significantly reduces the blurring in the radial and tangential blurring direction compared to Fig. 5(b). The greatest improvement is given by the deconvolution method, shown in Fig. 5(d). Both the radial and tangential blurring are significantly reduced. The resolution of the different methods applied to all four beads is quantitatively represented in Table 1.

We determined the sharpness metric and the SNR for the transverse slice reconstructed with all four methods. The lowest sharpness is given by the FBP with a value of 0.05. The PSF-based reconstruction has a value of 0.0794. The deconvolution shows a sharpness value of 0.18, and the FDR has a sharpness value of 0.19. For all methods, the SNR of the beads is quite similar. The PSF-based method has an SNR of 29.9. The SNR of the FDR method is 29.2 dB, the FBP of 32.6 dB, and the deconvolution has the highest SNR with 35.2 dB.

Table 1. FWHM Resolution (μm) in Radial Direction for the FBP, the Analytical FDR, Deconvolution and the PSF-Based Reconstruction for Four Fluorescent Beads[a]

		Bead			
Method	**Direction**	**1**	**2**	**3**	**4**
FBP	Radial	27.4 ± 0.3	8.9 ± 0.1	10.8 ± 0.1	8.3 ± 0.1
	Tangential	57.1 ± 0.6	17.3 ± 0.3	42.6 ± 0.3	35.4 ± 0.5
FDR	Radial	25.1 ± 0.4	5.1 ± 0.1	8.48 ± 0.5	6.975 ± 0.1
	Tangential	60.9 ± 1.2	18.2 ± 0.5	41.5 ± 0.6	36.8 ± 0.9
Deconvolution	Radial	7.5 ± 0.1	3.8 ± 0.1	5.9 ± 0.1	3.8 ± 0.1
	Tangential	23.3 ± 0.3	7.7 ± 0.2	10.2 ± 0.1	8.4 ± 0.1
PSF-based	Radial	19.1 ± 0.2	7.2 ± 0.2	8.5 ± 0.1	6.4 ± 0.1
	Tangential	33.8 ± 0.4	10.1 ± 0.3	25.4 ± 0.3	24.3 ± 0.4

[a]The errors indicate 95% confidence intervals.

A second comparison of the reconstruction algorithms is done using OPT imaging of a 10-day-old transgenic zebrafish larva to illustrate the performance on a biological sample. The zebrafish cellular membranes are labeled with green fluorescent protein. The zebrafish larva is euthanized in ice water at the Erasmus Medical Center, Rotterdam according to animal welfare regulations. Animal experiments are approved by the Animal Experimentation Committee of the Erasmus MC, Rotterdam.

The zebrafish is embedded in agarose and mounted in our OPT system [10]. The same experimental parameters are used as for the fluorescent bead data; however, the NA of the system is 0.027, which is lower than for the fluorescent beads. For the zebrafish imaging, a total of 1691 sinograms are acquired covering a distance of 6.5 mm along the rotation axis. For all 1691 slices, the tomographic image is reconstructed using FBP, FDR, deconvolution, and the PSF-based approach (no slice averaging). The measured data is preprocessed as described in [11]. Furthermore, the result of the FDR reconstruction is masked for visualization purposes by the average mask used for the SNR estimation.

A qualitative comparison of transversal slices through the zebrafish belly and tail is shown in Fig. 6 for the four different reconstruction techniques. Compared to FBP, deconvolution shows a small improvement in intensity and sharpness. The FDR has a much higher contrast and shows fewer artifacts in between the important biological structures. The PSF-based reconstruction shows the highest intensity and the least artifacts. Figures 6(b) and 6(c), show cross sections through parts of the zebrafish belly and tail from which similar conclusions can be drawn.

A comparison of a coronal slice of the zebrafish reconstructed with the different algorithms is shown in Fig. 7 (center). For this slice, a similar conclusion can be drawn as for the transversal slice. Only visually, deconvolution seems to perform better than the FDR.

Quantitative comparison of the SNR along the length of the zebrafish shows, see Fig. 7 (left), that FBP has the lowest SNR. The deconvolution method and the FDR have almost the same SNR, and the PSF-based reconstruction has the highest SNR, which is almost 10 dB better than the other reconstruction techniques. The sharpness of the image shows a similar

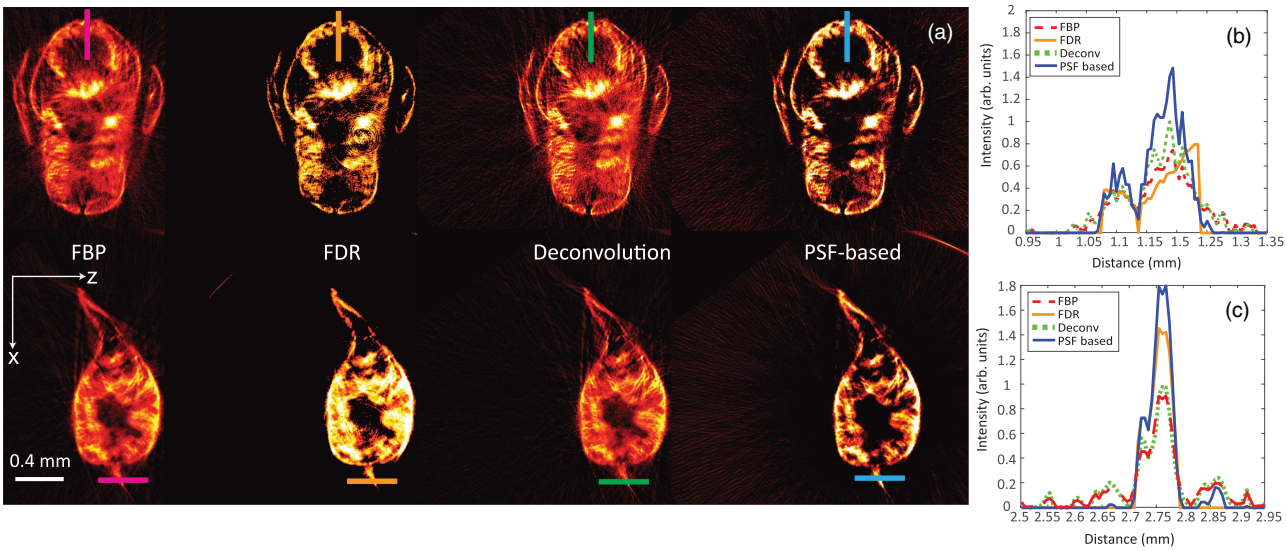

Fig. 6. (a) OPT image reconstructions of a single transverse slice of the zebrafish with the four reconstruction techniques, as indicated. (b) Cross section of the reconstructed intensity in the tangential direction through the zebrafish belly, and (c) cross section in radial direction through the zebrafish tail.

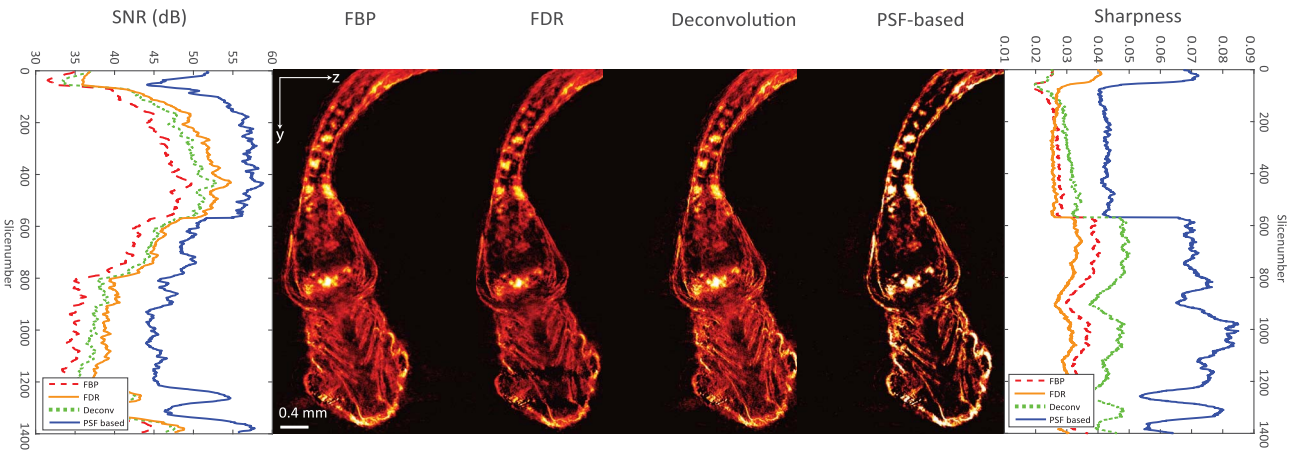

Fig. 7. Blind image quality comparison of the different reconstruction algorithms applied to OPT zebrafish imaging. (left) Signal-to-noise ratio versus slice number. (center) A single coronal slice through the zebrafish reconstructed with the four different reconstruction algorithms. The different reconstruction methods are indicated in the legend. (right) Sharpness versus slice number.

behavior, shown in Fig. 7 (right). In general, the FDR and the FBP have the lowest sharpness value. The sharpness of the deconvolution method is higher, and the PSF-based reconstruction approach yields the highest sharpness value. The jump in SNR and sharpness at slice 580 is due to the transition between the tail and the main body of the fish, where two datasets were fused.

5. DISCUSSION

We compare three different state-of-the-art tomographic reconstruction methods that reduce space-variant tangential blurring introduced by the optical imaging system with the classical FBP. We applied the algorithms to simulated data and experimental data of fluorescent beads and a zebrafish larva.

The deconvolution and PSF-based method give the best reconstruction results on simulated point source data. Especially for high NA imaging systems, they perform better than FDR. We attribute this to the fact that the FDR inverse filter is an approximation that is only exact if the OTF of the imaging system varies slowly over the rotation angle [8]. For this condition, the stationary phase approximation holds, and a simple expression for the inverse filter can be derived. Especially for high NA optical imaging systems, this condition is not met. Consequently, the derived FDR filter is incorrect. Furthermore, in case of noisy data, the FDR filter in the Fourier domain has regions, where a division is performed by values close to zero. This leads to an amplification of the noise, which is a common problem in inverse filtering [18]. If further regularization of the FDR is applied, we expect that the reconstruction result can be improved. Another improvement can be achieved by additional filtering of the sinogram, for example by a Wiener filter, which can reduce noise amplification of the inverse filter [9]. The PSF-based reconstruction is regularized indirectly by termination of the reconstruction after the most optimal number of iterations. Hence, it is therefore more robust to noise than the conventional FDR. Additional regularization of PSF-based reconstruction, such as Tikhonov or total variation minimization, could lead to less noise amplification and faster convergence. In that case, we expect that the absolute error for the PSF-based approach would remain constant after reaching the minimum reconstruction error.

The experimental data of the fluorescent beads demonstrates that the deconvolution algorithm shows the best performance for sparse and low SNR objects. Since the optimization landscape of the PSF-based approach for sparse and low SNR objects is very flat and noisy, many iterations are necessary to find a good and improved solution. Consequently, if the SNR would be higher for the bead data, the PSF-based method should be able to reduce the blurring to a similar level as deconvolution in a more useful timeframe, i.e., in fewer iterations. To enhance the convergence speed for sparse objects, more prior information can be included in the reconstruction; for example, an initial guess that is close to the real solution could lead to better reconstruction results.

For extended and nonsparse objects, such as the zebrafish larva, the PSF-based algorithm gives the best results, followed by the deconvolution approach. We attribute the good performance of the PSF-based algorithm to the fact that the intensities coming from an entire Gaussian-shaped region are correctly attributed to the measured projections. Hence, signal inconsistencies with the FBP reconstruction are removed, resulting in higher peak signals and a lower (noisy) background. Since for nonsparse objects the total object signal is higher, we observe fast convergence to the optimal result.

Obviously, analytical methods such as FBP, FDR, and deconvolution require little computation time. Considering potential improvements in computer power and improved coding of algorithms, we have focused on the obtained image quality and not considered reconstruction run time in our comparison of the different algorithms. However, for applications that require fast image reconstructions, a choice may be made for faster methods such as FBP, FDR, or deconvolution at the expense of a lower image quality. Moreover, for the PSF-based reconstruction, the user needs to make a few choices such as the maximum number of iterations and the tolerance of the

method to obtain optimal results. Although we choose the number of iterations after visual inspection, the selection of the maximum number of iterations can be automated during the reconstruction process using the NR-IQA image quality metrics presented here.

In this work we focused on the image quality improvement of tangential and radial blurring in OPT image reconstruction. The image quality is defined by the FWHM of point-like objects, as well as the SNR and a sharpness metric. Multiple factors influence which reconstruction technique performed best, such as sparsity in the image domain, the NA of the imaging lens, and the SNR of the imaged object. As a recommendation, we advise to reconstruct sparse objects in almost all cases with deconvolution. In cases where the PSF cannot be described by a simple analytical expression, we recommend the PSF-based reconstruction, which gives similar results for high SNR data. For low NA tomographic imaging of nonsparse objects, we recommend the PSF-based reconstruction, as it gives superior image quality.

6. CONCLUSION

In this paper, we compared various tomographic image reconstruction techniques that take the PSF into account. For high SNR and nonsparse objects, the PSF-based reconstruction yields superior performance. For sparse objects, deconvolution shows the best performance.

Funding. Dutch Technology Foundation TTW, Nederlandse Organisatie voor Wetenschappelijk Onderzoek (NWO), which is partly funded by the Ministry of Economic Affairs.

REFERENCES

1. E. Wolf, "Three-dimensional structure determination of semi-transparent objects from holographic data," Opt. Commun. **1**, 153–156 (1969).
2. J. Sharpe, U. Ahlgren, P. Perry, B. Hill, A. Ross, J. Hecksher-Sørensen, R. Baldock, and D. Davidson, "Optical projection tomography as a tool for 3D microscopy and gene expression studies," Science **296**, 541–545 (2002).
3. A. C. Kak and M. Slaney, *Principles of Computerized Tomographic Imaging* (IEEE, 1988).
4. E. Rapisarda, V. Bettinardi, K. Thielemans, and M. C. Gilardi, "Image-based point spread function implementation in a fully 3D OSEM reconstruction algorithm for PET," Phys. Med. Biol. **55**, 4131–4151 (2010).
5. R. Formiconi, A. Pupi, and A. Passeri, "Compensation of spatial system response in SPECT with conjugate gradient reconstruction technique," Phys. Med. Biol. **34**, 69–84 (1989).
6. Z. Chen and R. Ning, "Three-dimensional point spread function measurement of cone-beam computed tomography system by iterative edge-blurring algorithm," Phys. Med. Biol. **49**, 1865–1880 (2004).
7. B. Recur, J. P. Guillet, I. Manek-Hönninger, J. C. Delagnes, W. Benharbone, P. Desbarats, J. P. Domenger, L. Canioni, and P. Mounaix, "Propagation beam consideration for 3D THz computed tomography," Opt. Express **20**, 5817–5829 (2012).
8. W. Xia, R. M. Lewitt, and P. R. Edholm, "Fourier correction for spatially variant collimator blurring in SPECT," IEEE Trans. Med. Imaging **14**, 100–115 (1995).
9. J. R. Walls, J. G. Sled, and J. Sharp, "Resolution improvement in emission optical projection tomography," Phys. Med. Biol. **52**, 2775–2790. (2007).
10. J. van der Horst and J. Kalkman, "Image resolution and deconvolution in optical tomography," Opt. Express **24**, 24460–24472 (2016).
11. A. K. Trull, J. van der Horst, W. J. Palenstijn, L. J. van Vliet, T. van Leeuwen, and J. Kalkman, "Point spread function based image reconstruction in optical projection tomography," Phys. Med. Biol. **62**, 7784–7797 (2017).
12. J. Radon and P. Parks, "On the determination of functions from their integral values along certain manifolds," IEEE Trans. Med. Imaging **5**, 170–176 (1986). Translation of the original paper by Johann Radon 1917.
13. S. J. Glick, B. C. Penny, M. A. King, and C. L. Byrne, "Noniterative compensation for the distance-dependent detector response and photon attenuation in SPECT imaging," IEEE Trans. Med. Imaging **13**, 363–374 (1994).
14. R. M. Lewitt, P. R. Edholm, and W. Xia, "Fourier method for correction of depth-dependent collimator blurring," Proc. SPIE **1092**, 232–243 (1989).
15. Z. Wang and A. Bovik, *Modern Image Quality Assessment* (Morgan and Claypool/Academic, 2006), pp. 1–15.
16. R. Gonzalez and R. Woods, *Digital Image Processing* (Pearson, 2008).
17. K. De and V. Masilamani, "Image sharpness measure for blurred images in frequency domain," Procedia Eng. **64**, 149–158 (2013).
18. B. Jahne, *Computer Vision and Applications: A Guide for Students and Practitioners* (Academic, 2000).